High Resolution Topography of 6 km of the Lost River Fault and 1983 Mw6.9 Borah Peak Earthquake Surface Rupture Near Doublespring Pass Road, Idaho, USA

Michael P. Bunds[1] (michael.bunds@uvu.edu), Christopher B. DuRoss[2], Ryan D. Gold[2], Nadine G. Reitman[2,3], Nathan A. Toké[1], Richard W. Briggs[2], Brittany Ungerman[1], and Ephram Matheson[1]

[1] Dept. of Earth Science, Utah Valley University, 800 West University Parkway, Orem, UT 84058
[2] U.S. Geological Survey, 1711 Illinois Street, Golden, CO 80401
[3] University of Colorado Boulder, UCB 399, Boulder, CO 80309-0399

DOI:

Introduction

Georeferenced, high resolution topography (HRT) was acquired for ~6.1 km of surface rupture from the 1983 Mw6.9 Borah Peak Earthquake on the Lost River fault near Doublespring Pass Road in the northeastern Basin and Range, Idaho, USA. Two point clouds, digital surface models (DSMs) and orthomosaics were generated from low-altitude aerial photographs using Structure-from-Motion and multi-view stereo processing (SfM) (Table 1). One set of HRT covers ~5.1 km of fault strike at Doublespring Pass Road, and the second covers ~1.0 km of fault at Poison Spring which is ~3 km north of Doublespring Pass Road. The data are available free-to-public on OpenTopography. An overview of the datasets and methods used to create it are provided here.

For additional information, please contact Michael Bunds, Utah Valley University (michael.bunds@uvu.edu).

Background

The Lost River fault zone (LRFZ) is a range-bounding, west-dipping normal fault in the northern Basin and Range province (Figure 1). The Mw 6.9 1983 Borah Peak earthquake occurred on it and created surface rupture along the southern portion of the Warm Spring section and the entire Thousand Springs section of the fault (Crone et al., 1987; DuRoss et al., 2019). Doublespring Pass Road (DSP) crosses the fault near the center of the Thousand Springs section. At DSP the surface rupture is well exposed and preserved, and it is very easily accessed. To the north of DSP, the surface rupture trends into a salient of limestone and complexly bifurcates into multiple strands ('West Spring Block' of Crone et al., 1987). North of the salient, at a site informally named Poison Spring (PS; West Spring in Crone et al., 1987), the surface rupture becomes localized again, with most displacement concentrated onto a single strand. Paleoseismic investigations have been conducted near both DSP (Hait and Scott, 1978; Schwartz and Crone, 1985) and PS (Vincent, 1995). The target sites of the data presented here were the surface rupture at DSP. We used small unoccupied aerial systems (sUAS) to acquire aerial photographs, which were georeferenced with ground control points to create point clouds. The point clouds model the topography at high resolution ($\leq$ 10 cm) along a ~6.1 km length of the fault.

Georeferenced, high resolution topography of the northern ~16.4 km of surface rupture on the Lost River fault is also publicly available from OpenTopography under a separate DOI (Bunds et al., 2019, 10.5069/G9222RWR).

Data Description (Table 1)

1. Two point cloud models

a. The DSP point cloud contains 1.272 x 10^9 points, each with a color attribute. Points are unclassified and include both ground and vegetation. The point cloud covers approximately 3.6 km^2, for an average point density of 354 points/m^2. The reference frame for the point cloud and all associated data is NAD83(2011) UTM zone 12 (EPSG 6341), epoch 2010.000, and the vertical datum is NAVD88 (orthometric heights determined using GEOID 12B, units of meters).
b. The PS point cloud contains 484 x 10^6 points, each with a color attribute. Points are unclassified and include both ground and vegetation. The point cloud covers approximately 0.61 km^2, for an average point density of 793 points/m^2. The reference frame for the point cloud is NAD83(2011) UTM zone 12 (EPSG 6341), epoch 2010.000, and the vertical datum is NAVD88 (orthometric heights determined using GEOID 12B, units of meters).

2. Two digital surface models (DSMs), both with a 0.10 m pixel size. The DSMs were derived from the point clouds and cover the same areas. Rasterization was performed in Agisoft Metashape (v1.5.1), using a 'binning' algorithm, wherein each DSM pixel value (elevation) is calculated as an average of the elevations of points located within the pixel area (averages of ~3.5 and 7.9 points per pixel for the two DSMs). The reference frame for the DSMs is the same as the point cloud, NAD83(2011) UTM zone 12 (EPSG 6341), epoch 2010.000, and NAVD88 (i.e., orthometric heights determined using GEOID 12B, units of meters).
3. Orthomosaics, with 0.05 (DSP) and 0.025 (PS) m pixel size. The orthomosaics were constructed from the aerial imagery in Agisoft Metashape, using the DSM to project the imagery. The reference frame is the same as the other data, NAD83(2011) UTM zone 12 (EPSG 6341), epoch 2010.000.
4. Table of camera locations. The point clouds were constructed from low-altitude aerial photographs taken from a sUAS. Tables of the locations from which aerial photographs were taken are provided as comma-delimited files. The reference frame is NAD83(2011) UTM zone 12 (EPSG 6341), epoch 2010.000, and NAVD88 (i.e., orthometric heights determined using GEOID 12B, units of meters). Camera positions and altitudes were estimated during SfM processing in Agisoft Metashape.
5. Table of ground control point locations. The point clouds were georeferenced using ground control points (GCPs), which are markers placed on the ground and the positions of which were surveyed with differential GNSS (see georeferencing section below). Tables of the locations of the GCPs are provided as comma-delimited files. The reference frame is NAD83(2011) UTM zone 12 (EPSG 6341), epoch 2010.000, and NAVD88 (i.e., orthometric heights determined using GEOID 12B, units of meters).
6. Tables of check point locations. Checkpoints were measured and used to assess the vertical uncertainty of the modeled topography (see georeferencing section below). Checkpoints were measured on relatively flat, bare ground, away from vegetation using dGNSS. Tables of the checkpoint locations are provided as comma-delimited files. The reference frame is NAD83(2011) UTM zone 12 (EPSG 6341), epoch 2010.000, and NAVD88 (i.e., orthometric heights determined using GEOID 12B, units of meters).

Data Collection Overview

Field work to acquire the high-resolution topography was conducted in May 2015 and May 2016, and followed the methods of Bunds et al. (2015) and DuRoss et al. (2019). The DSP survey area was divided

into 3 subsections ('polygons') to organize field work and facilitate processing. Two polygons were flown in 2015, one in 2016. The area flown in 2016 comprises the southern part of the surveyed area. Each polygon contains at least nine ground control points and the polygons were designed to overlap each other, so that photographs and GCPs are shared between adjacent polygons where possible. The PS area was surveyed as a single polygon in May, 2016.

The DSP point cloud model was made from total of 3212 low altitude aerial photographs. In 2015, DJI Phantom 2 v2 quadcopters equipped with Sony A5100 cameras (16 mm prime lens) using a custom, fixed mount were used. A Falcon fixed wing also equipped with a Sony A5100 (20 mm prime lens) was used in 2016 to fly the southern portion of the area. The fixed camera mount (as opposed to a gimbal), caused the camera orientation to change with the orientation of the sUAS, and to vary from nadir by up to ~35°. Average photograph ground sample distance (GSD) is ~2.84 cm. At DSP, the DJI Phantom was flown considerably lower (mostly 60 – 120 m above ground level [agl]) than the Falcon (mostly 160 – 388 m agl), and consequently there is a large variation in GSD. In addition, the large difference in photograph acquisition created some small areas of poor topographic reconstruction. Photograph overlap as calculated by Agisoft is > 9 throughout most of the survey area, with the exception of portions of the southern half. Areas that lack sufficient overlap may have poorer quality reconstruction which can be evident in the resulting model. An additional measure of overlap is the number of photographs in which GCPs appear, which averages 17.7 photographs/GCP (DSP; minimum = 6).

The PS point cloud model was made from 1379 low altitude aerial photographs. As for the northern portion of the DSP area, an DJI Phantom 2 v2 quadcopter equipped with Sony A5100 camera (16 mm prime lens) using a custom, fixed mount was used to collect the imagery. The fixed camera mount caused the camera orientation to vary from nadir by up to ~31°. Average photograph ground sample distance (GSD) is ~2.39 cm. Photograph overlap as calculated by Agisoft is > 9 throughout nearly the entirety of the mapped area. Areas that lack sufficient overlap may have poorer quality reconstruction which can be evident in the resulting model. GCPs appear in an average of 46.1 photographs each, reflecting generally excellent overlap. The target of the mapping was the surface rupture and GCPs were only placed near it, whereas imagery was collected over a wider area. Elevation accuracy should be expected to decrease outside of the area covered by the GCPs.

The DJI Phantom was piloted and navigated manually, without calculated, pre-determined flight plans generated by software or other means. The Falcon fixed-wing used for the southern portion of the DSP area flew autonomously along a pre-determined flight plan. The areas flown by each sUAS and method are readily evident in maps of camera locations. Photography was conducted under clear to partly cloudy skies at DSP, and under overcast skies and an intermittent light rain-snow mix at PS. Tables of positions for the photographs are included in the metadata. The camera positions are estimates calculated during SfM processing.

Processing

Processing was done with Agisoft Metashape v1.5.1 – v1.6.1 (see also DuRoss et al., 2019; Scott et al., 2020). Sparse clouds of ties points were generated in the first processing step. The sparse cloud was iteratively filtered to remove large uncertainty points and the model was re-optimized. A dense point cloud was then generated. The sparse point cloud and camera model was made using the 'high' setting in Agisoft (i.e., photos were downsampled by a factor of 2), and the dense cloud was built using the

'high' setting (i.e., photographs were downsampled x2). DSMs were made in Agisoft Metashape, which averaged elevations of points within each DSM pixel to calculate the pixel elevations.

Georeferencing and Accuracy

All data (point clouds, DSMs, orthomosaics, and accompanying GCP and camera locations), are in NAD83(2011) UTM Zone 12 (EPSG 6341) coordinates, with elevations given as NAVD88 orthometric heights in meters determined using GEOID 12B. All data were processed in epoch 2010.0000.

The point clouds were georeferenced using GCPs. GCPs consisted of markers placed on the ground, the positions of which were measured using differential GNSS (dGNSS). At DSP, 35 GCPs were used and 11 GCPs were used at PS. Tables of GCP positions are included.

dGNSS was done in kinetic mode using a local reference station and a single rover. The reference station consisted of a Trimble 5700 receiver and Trimble Zephyr Geodetic I antenna. The reference station locations were determined using the National Geodetic Survey's Online Positioning User Service (OPUS) and over 16 hours occupation time at DSP and three hours at PS. Reference station uncertainty for DSP is estimated to be approximately +/- 0.003 and 0.006 m horizontal and vertical respectively, and for PS is is approximately +/- 0.02 and 0.014 m horizontal and vertical respectively. A temporary survey marker was constructed at DSP in 2015 by pounding a ~ 1 m length of rebar into the ground and dimpling the top with a hammer drill. The survey marker was used in both 2015 and 2016 to minimize uncertainty in the precision of the data at that site. A Trimble R8 rover was used to occupy the GCPs (and checkpoints). Rover accuracy degrades slightly towards the east, where proximity to the Lost River Range limited satellite visibility and decreased measurement precision. GCP location measurement uncertainty is estimated to vary from +/- 0.01 (horizontal) and +/- 0.015 (vertical) up to approximately +/- 0.02 (horizontal) and +/- 0.035 (vertical).

The position of every GCP was manually marked by hand in every photograph in which it clearly appears using Agisoft Metashape prior to optimization of the sparse point clouds and camera models.

The final point clouds, DSMs and orthomosaics were cropped prior to export from Agisoft Metashape. Cropping was done to include only the areas reasonably well covered by GCPs and photographs.

Vertical accuracy of the final DSMs was assessed using checkpoints (Bunds et al., 2015). Checkpoints are dGNSS measurements taken on bare, relatively flat ground away from GCPs and vegetation, and within the area covered by GCPs and camera locations. At DSP, 109 checkpoints were used to confirm vertical accuracy, and at PS 14 checkpoints were measured. The elevation predicted for each checkpoint was extracted from the corresponding DSM using ArcMap, and a residual calculated as the difference between the DSM elevation and the directly measured elevation for each checkpoint. Root-mean-square error (RMSe; 1-sigma error) for checkpoints relative to the DSM at DSP is 6.6 cm, and at PS it is 7.1 cm. GCPs and checkpoints were measured using the same reference stations as the GCPs, so some additional error is likely to be present in the data set due to error in the absolute positions of the reference station, however based on the quality of the OPUS solutions this is likely to be small relative to the checkpoint RMSe. Note that misfit of the point clouds to GCPs (as measured by Agisoft) is much less than checkpoint error, and reflects the fact that GCP misfit as calculated in Agisoft is not a reliable measure of model accuracy across the survey area.

DSM and point cloud error should be expected to vary across the surveyed areas, and may deviate significantly from the estimate of average error provided by the checkpoint RMSe. Larger errors should be expected at large distances from GCPs; outside of the area covered by the GCPs, flight lines or good camera coverage; and in areas of poor model reconstruction. SfM processing using GCPs typically results in a model with good fit to GCPs, and potential warping between GCPs, as well as significant potential warping in areas not surrounded by GCPs (i.e., areas on the edge of the data set, outside of GCP coverage) (e.g., Bunds et al., 2015). For example, warping should be expected in the southernmost portion of the DSP data that extends beyond the southernmost GCPs. Photograph coverage and model reconstruction also affect error, and portions of the models that extend beyond flight lines are likely to contain larger than average error. There are areas in the data set with relatively poor camera coverage and reconstruction; it should be expected that error in these areas is greater than the overall RMSe. These areas are apparent in the DSM and derivatives made from it such as hillshades. The tables of GCP and camera locations are included to aid identification of areas prone to relatively large error. Lastly, although extensive efforts have been made to minimize and quantify error in the data set, no guarantee of accuracy is given nor implied.

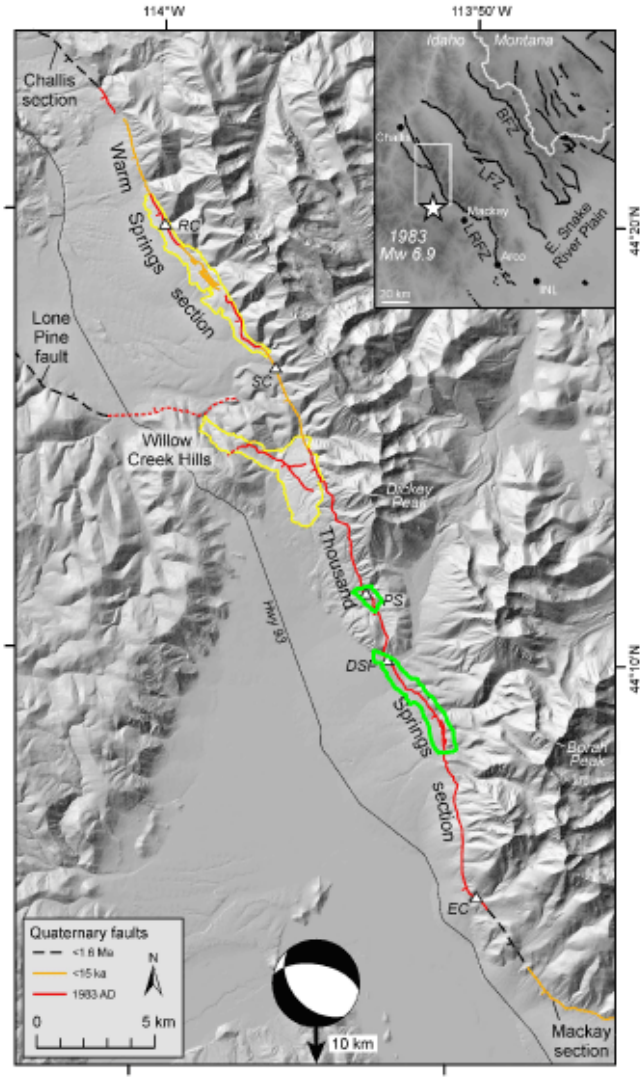

Figure 1. Location map showing approximate areas covered by the Doublespring Pass Road data set presented here (outlined in green), and data sets from nearby and available on OpenTopography. Faults from USGS Quaternary Fault and Fold Database, focal mechanism from Doser and Smith (1985), epicenter location from Richins et al., (1987). Figure modified after DuRoss et al. (in press).

Table 1. Summary of Topographic Model Parameters

Parameter	DSP Topographic model	PS Topographic model
Total points	1.273×10^9	484×10^6
Coverage area	3.6 km^2	0.61 km^2
Point density	354 points/m^2	793 points/m^2
Number photographs	3212	1379
Average GSD	0.0284 m	0.0239 m
Number GCPs	35	11
Number checkpoints	109	14
Checkpoint RMSerror	0.066 m	0.071 m
DSM resolution	0.10 m	0.10 m
Orthomosaic resolution	0.05 m	0.025 m
Horizontal reference frame – point clouds, DSMs and orthomosaics	NAD83(2011) UTM Zone 12 (EPSG 6341) epoch 2010.0000	NAD83(2011) UTM Zone 12 (EPSG 6341) epoch 2010.0000
Vertical reference frame	NAVD88 (GEOID12B)	NAVD88 (GEOID12B)
Field data collection date	May, 2015 and May, 2016	May, 2016

References Cited

Bunds, M.P., Toké, N., DuRoss, C., Gold, R., Reitman, N., Johnson, K., Lajoie, L., Personius, S., Briggs, R., Fletcher, A., 2015, High-Resolution Topographic Mapping for Geologic Hazard Studies Using Low-Altitude Aerial Photographs and Structure from Motion Software: Methods, Accuracy, and Examples, Geological Society of America Annual Meeting Abstracts with Program.

Bunds, M.P., DuRoss, C.B., Gold, R.D., Reitman, N.G., Toke, N.A., Briggs, R.W., Personius, S.F., Johnson, K., Lajoie, L., *Ungermann, B., Matheson, E., Andreini, J., Larsen, K.,* 2019, High Resolution Topography of the Northern 16 km of the M6.9 1983 Borah Peak Earthquake Surface Rupture on the Lost River Fault Zone, Idaho, USA, OpenTopography, DOI: 10.5069/G9222RWR

Bunds, M.P., DuRoss, C.B., and Reitman, N.G., 2019, High Resolution Topography of 1 km of the Lost River Fault and 1983 Mw6.9 Borah Peak Earthquake Surface Rupture at Poison Spring, Idaho, USA, OpenTopography, DOI: 10.xxx

Crone, A.J., Machette, M.N., Bonilla, M.G., Lienkaemper, J.J., Pierce, K.L., Scott, W.E., and Bucknam, R.C., 1987, Surface faulting accompanying the Borah Peak Earthquake and segmentation of the Lost River Fault, Central, Idaho, Bulletin of the Seismological Society of America, v.77, n. 3, pp 739-770.

Doser, D.I., and Smith, R.B., 1985, Source parameters of the 28 October 1983 Borah Peak, Idaho, earthquake from body wave analysis: Bulletin of the Seismological Society of America, v. 75, p. 1041–1051.

DuRoss, C.B., Bunds, M.P., Gold, R.D., Briggs, R.W., Reitman, N.G., Personius, S.F., Toke, N.A., 2019, Variable normal-fault rupture behavior, northern Lost River fault zone, Idaho, USA, Geosphere, v 15, https://doi.org/10.1130/GES02096.1.

Hait, M.H., Jr., and Scott, W.E., 1978, Holocene faulting, Lost River Range, Idaho, Geological Society of America Abstracts with Programs, v. 10, p. 217.

Richins, W.D., Pechmann, J.C., Smith, R.B., Langer, C.J., Goter, S.K., Zollweg, J.E., and King, J.J., 1987, The 1983 Borah Peak, Idaho, earthquake and its aftershocks: Bulletin of the Seismological Society of America, v. 77, p. 694–723.

Schwartz, D.P. and Crone, A.J., 1985, The 1983 Borah Peak earthquake: A calibration event for quantifying eqarthquake recurrence and fault behavior of Great Basin normal faults, in Stein, R.S. and Bucknam, R.C., eds., Proceedings of Workshop XXVIII on the Borah Peak, Idaho, Earthquake: U.S. Geological Survey Open-File Report 85-290, v. A, p. 153-160.

Scott, C., Bunds, M.P., Shirzaei, M., Toke, N., 2020, Creep along the Central San Andreas Fault from Surface Fractures, Topographic Differencing, and InSAR Imagery, Journal of Geophysical Research, https://doi.org/10.1029/2020JB019762.

U.S. Geological Survey, 2018, Quaternary Fault and Fold Database of the United States, https://earthquake.usgs.gov/hazards/qfaults/, accessed September 2018.

Vincent, K.R., 1995, Implications for models of fault behavior from earthquake surface-displacement along adjacent segments of the Lost River fault, Idaho, Ph.D. thesis, Tuscon, Arizona, University of Arizona, 152 pp.

Acknowledgements

We thank the U.S. Geological Survey Unmanned Aircraft Systems (UAS) Project, including Jeff Sloan, Mark Bauer, Joe Adams, and Todd Burton for conducting a Falcon flight the provided photographs for this project. We also thank Kendra Johnson and Lea Lajoie for discussions on UAS photography and high resolution topography production methods. This work was supported by awards from the Scholarly Activities Committee in the College of Science, Utah Valley University. We are grateful to NVIDIA Corporation for providing computing support through their Graphic Processing Unit (GPU) Grant Program.